AGU PUBLICATIONS

JGR

Journal of Geophysical Research: Oceans

RESEARCH ARTICLE

10.1002/2015JC011223

Key Points:
- The ISV of thermocline is dominated by remote forcing from the equatorial Indian Ocean wind stress
- The ISV of SST is dominated by upwelling induced by remote equatorial wind during summer-fall
- The ISV of SST results from shortwave radiation and turbulent heat flux during winter-spring

Supporting Information:
- Supporting Information S1

Correspondence to:
G. Chen,
chengengxin@scsio.ac.cn; D. Wang,
dxwang@scsio.ac.cn

Citation:
Chen, G., W. Han, Y. Li, D. Wang, and T. Shinoda (2015), Intraseasonal variability of upwelling in the equatorial Eastern Indian Ocean, *J. Geophys. Res. Oceans*, *120*, 7598–7615, doi:10.1002/2015JC011223.

Received 13 AUG 2015
Accepted 27 OCT 2015
Accepted article online 30 OCT 2015
Published online 20 NOV 2015

Intraseasonal variability of upwelling in the equatorial Eastern Indian Ocean

Gengxin Chen[1,2], Weiqing Han[2], Yuanlong Li[2], Dongxiao Wang[1], and Toshiaki Shinoda[3]

[1]State Key Laboratory of Tropical Oceanography, South China Sea Institute of Oceanology, Chinese Academy of Sciences, Guangzhou, China, [2]Department of Atmospheric and Oceanic Sciences, University of Colorado, Boulder, Colorado, USA, [3]Department of Physical and Environmental Sciences, Texas A&M University–Corpus Christi, Corpus Christi, Texas, USA

Abstract By analyzing satellite observations and conducting a series of ocean general circulation model experiments, this study examines the physical processes that determine intraseasonal variability (ISV) of the equatorial eastern Indian Ocean (EIO) upwelling for the 2001–2011 period. The ISV of EIO upwelling—as indicated by sea level, thermocline depth, and sea surface temperature (SST)—is predominantly forced by atmospheric intraseasonal oscillations (ISOs), and shows larger amplitudes during winter-spring season (November–April) when atmospheric ISOs are stronger than summer-fall (May–October). The chlorophyll (Chl-a) concentration, another indicator of upwelling, however reveals its largest intraseasonal variability during May–October, when the mean thermocline is shallow and seasonal upwelling occurs. For both winter-spring and summer-fall seasons, the ISV of EIO sea level and thermocline depth is dominated by remote forcing from the equatorial Indian Ocean wind stress, which drives Kelvin waves that propagate along the equator and subsequently along the Sumatra-Java coasts. Local wind forcing within the EIO plays a secondary role. The ISV of SST, however, is dominated by upwelling induced by remote equatorial wind only during summer-fall, with less contribution from surface heat fluxes for this season. During winter-spring, the ISV of SST results primarily from shortwave radiation and turbulent heat flux induced by wind speed associated with the ISOs, and local forcing dominates the SST variability. In this season, the mean thermocline is deep in the warm pool and thus thermocline variability decouples from the ISV of SST. Only in summer-fall when the mean thermocline is shallow, upwelling has important impact on SST.

1. Introduction

In the equatorial Pacific and Atlantic Oceans, easterly trade winds prevail and upwelling occurs in the eastern equatorial cold tongue region. By contrast, in the equatorial Indian Ocean annual mean surface winds are westerlies, and the warm pool occupies the equatorial Eastern Indian Ocean (EIO) where the mean thermocline is usually deep (Figure 1f). The mean upwelling zone is located at the southwestern basin thermocline ridge region between 12°S and 2°S, and it is driven by the wind stress curl associated with the westerlies near the equator and easterly trades south of ~10°S [*McCreary et al*., 1993; *Murtugudde and Busalacchi*, 1999]. Even though the EIO resides in the warm pool, upwelling still occurs in boreal summer-fall season especially during the Indian Ocean Dipole (IOD) years [*Saji et al*., 1999; *Webster et al*., 1999; *Murtugudde et al*., 2000]. Upwelling in the EIO alters the warm pool sea surface temperature (SST) and modifies tropical deep convection, inducing anomalous atmospheric circulation and therefore impacting regional and global climate [e.g., *Sardeshmukh and Hoskins*, 1988; *Webster and Lukas*, 1992; *Yu et al*., 2002; *Wang and Mehta*, 2008; *Izumo et al*., 2010; *Kim et al*., 2012]. In this paper, seasons refer to those of the northern hemisphere.

On seasonal timescales, the strong, local southeast monsoon winds cause upwelling in the EIO from June to October, shoaling the thermocline (represented by D20—the depth of 20°C isotherm), lowering sea surface height (SSH), cooling SST, and increasing chlorophyll (Chl-a) concentration [e.g., *Susanto et al*., 2001]. Meanwhile, the remote equatorial zonal winds in the interior Indian Ocean exhibit strong semiannual variability [e.g., *Wyrtki*, 1973], shoaling D20 during January–March and July–September when equatorial easterly winds prevail. The shallow D20 signals propagate into the EIO via equatorial Kelvin waves, intensifying the seasonal upwelling and cold SST anomalies (SSTA) induced by the local monsoon during summer-fall season (May–October; Chen et al. Interannual variability of Eastern Indian Ocean upwelling: Local versus remote forcing, submitted to *Journal of Physical Oceanography*, 2016) During winter-spring (November–April),

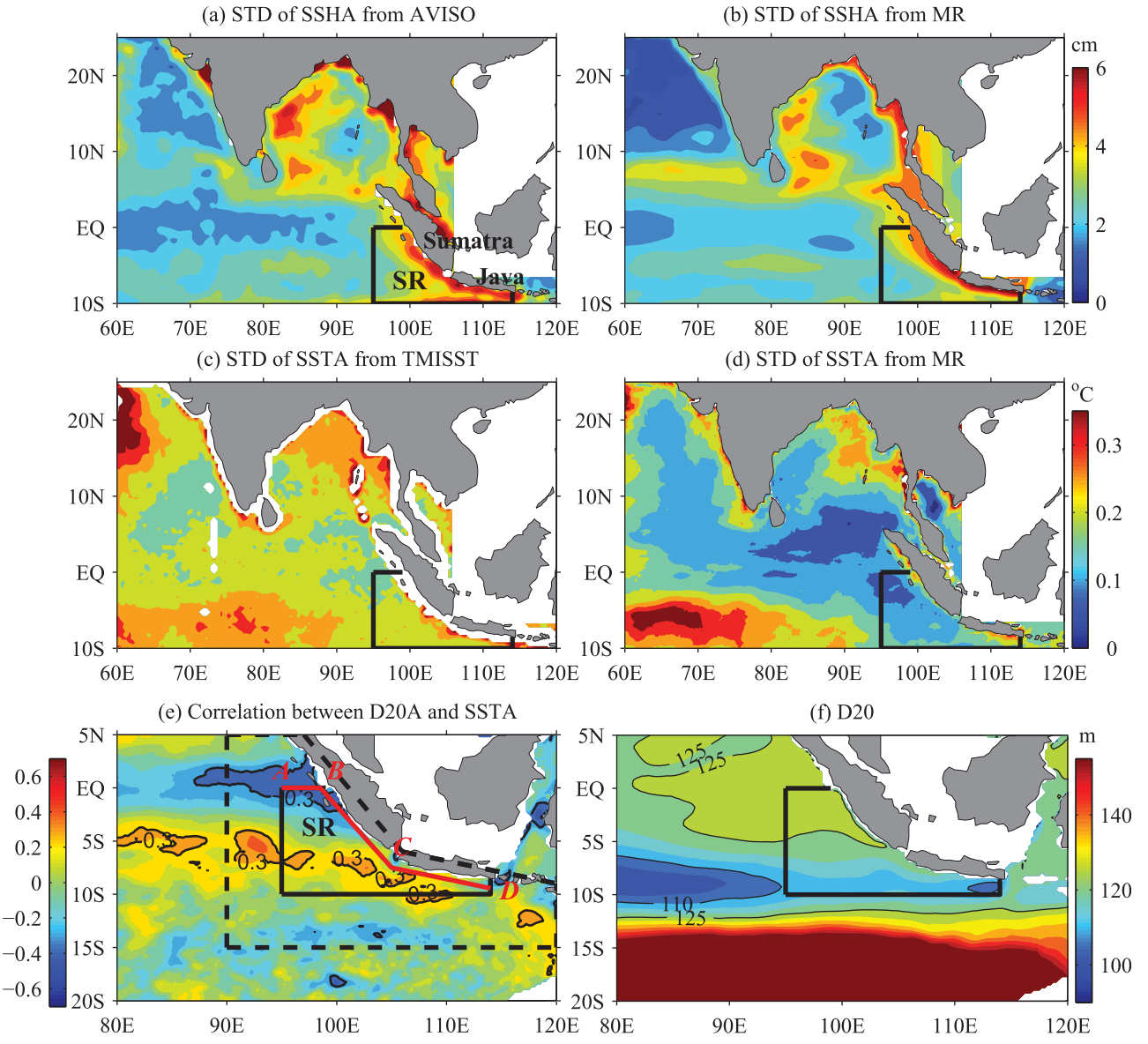

Figure 1. The STD maps of intraseasonal (30–105 day band-pass filtered) (a) SSHA from AVISO, (b) SSHA from HYCOM MR, (c) SSTA from TMISST, and (d) SSTA from HYCOM MR. The black box shows the study region (SR) of the EIO that covers the (95°E–114°E, 10°S–0°N), which is approximately the eastern antinode region of the IOD (90°E–110°E, 10°S–0°N). (e) Correlation map between intraseasonal SSTA and D20A from 2001 to 2011. The regions between SR and dashed-black lines mark the transition regions of HYCOM experiment runs, where the real forcing gradually changes to no ISO forcing in the SR. The red line is used to show propagation of Kelvin waves along the equator (from 95°E at location A) and along the coasts of Sumatra and Java, with letters A–D showing the start, turn and end positions. (f) Distribution of the climatological D20 averaged for 2001–2011.

however, the EIO SSTAs may decouple from D20 anomalies (D20A) because of the deep thermocline there. This situation differs markedly from the cold tongue upwelling over the eastern equatorial Pacific and Atlantic, where D20As have good agreements with SSTAs [e.g., *Zelle et al.*, 2004]. Because of its uniqueness, the EIO upwelling has been identified as one of the research priorities by the CLIVAR Indian Ocean Panel of the World Climate Research Program, and the EIO upwelling research initiative has been proposed to understand the EIO upwelling dynamics and ecosystem impacts (see CLIVAR/IOC-GOOS Indian Ocean Region Panel Achievements and Future Plans at http://www.clivar.org/clivar-panels/indian).

On interannual timescales, the EIO upwelling is related to the IOD and El Niño and the Southern Oscillation (ENSO) events [*Saji et al.*, 1999; *Webster et al.*, 1999; *Murtugudde et al.*, 2000]. By separately suppressing interannual wind forcing east and west of 90°E, *Murtugudde et al.* [2000] concluded that the SSTA off Sumatra for the 1997–1998 IOD event was forced roughly equally by local alongshore winds and remote equatorial winds. Chen et al. (submitted manuscript, 2016) quantified the remote versus local forcing in causing

interannual variability of the EIO upwelling from 2001 to 2011 and elucidated the associated processes. They found that interannual variability of D20 in the EIO, as the primary indicator of upwelling, is dominated by remote forcing from the equatorial winds, whereas interannual variability of SST results mainly from local forcing, with different processes dominating the SSTA during summer-fall and winter-spring seasons.

In addition to seasonal-to-interannual variability, winds and other surface forcing fields over the tropical Indian Ocean present large amplitude intraseasonal variability (ISV), which is associated with atmospheric intraseasonal oscillations (ISOs) with the dominant mode being the Madden-Julian Oscillation (MJO) [e.g., *Madden and Julian*, 1971; *Hendon and Glick*, 1997; *Webster et al*., 2002]. Extensive observational and modeling studies are conducted for understanding the response of equatorial Indian Ocean (e.g., current, SSH, SST, and D20) to atmospheric intraseasonal forcing [e.g., *McPhaden*, 1982; *Shinoda and Hendon*, 1998; *Shinoda et al*., 1998; *Reppin et al*., 1999; *Han et al*., 2001, 2004, 2007; *Sengupta et al*., 2001; *Schouten et al*., 2002; *Schiller and Godfrey*, 2003; *Senan et al*., 2003; *Waliser et al*., 2003, 2004; *Han*, 2005; *McPhaden and Foltz*, 2013; see *Schott et al*., 2009 for a review and references therein]. Intraseasonal equatorial Kelvin waves driven by winds associated with the MJO can propagate into the Indonesian Seas [*Qiu et al*., 1999; *Iskandar et al*., 2005, 2006], affecting ISV of sea level in different seasons along Sumatra and Java coasts [*Iskandar et al*., 2005] and the Indonesian Throughflow at the straits of Lombok, Ombai, and Timor [*Schiller et al*., 2010] and at the Makassar Strait [*Pujiana et al*., 2013].

While ISV of the equatorial Indian Ocean has been extensively studied, and intraseasonal equatorial Kelvin waves have been shown to affect the Indonesian Seas, a comprehensive study that focuses on investigating the ISV of EIO upwelling system has not yet been reported. Particularly, the relative importance of remote and local forcing on the EIO upwelling at intraseasonal timescales has not been quantified, even though the influence of remote and local forcing on ISV of the Indonesian seas has been verified [e.g., *Qiu et al*., 1999; *Iskandar et al*., 2005; *Schiller et al*., 2010]. In this paper, we investigate the physical processes that determine ISV of the EIO upwelling, which can be represented by various upper ocean fields, and quantify the influences of remote forcing from the equator and local forcing within the EIO. Specifically, we examine how the remote and local forcing affect ISV of the EIO SSH, D20 and SST during summer-fall upwelling season, and assess the relative importance of surface shortwave radiation (SWR), surface turbulent heat fluxes, and oceanic processes (dynamics and mixed layer physics) in causing intraseasonal SSTA. As a comparison, ISV of the EIO during winter-spring season will also be examined. Our period of interest is 2001–2011, when high-quality satellite observations are available for forcing the ocean model.

The rest of the paper is organized as follows. Section 2 describes data, model, and experiments. Section 3 verifies the model performance, and investigates processes controlling the EIO upwelling on intraseasonal timescales. Section 4 provides a summary and discussion. Results from this study will advance our understanding of ISV of oceanic biological productivity and its seasonality in the EIO upwelling system, and benefit our understanding of air-sea interaction processes associated with the MJO [*Webber et al*. 2012] given that intraseasonal SSTA can affect atmospheric deep convection in the warm pool region.

2. Data, Ocean Model, and Experiments

2.1. Data

The Tropical Rainfall Measuring Mission Microwave Imager SST (TMISST) products are available since December 1997 with a horizontal resolution of $0.25^\circ \times 0.25^\circ$ [*Wentz et al*. 2000]. In this study, the daily SST data from 1 January 2001 to 29 November 2011 are used to analyze ISV of SST. The daily $0.25^\circ \times 0.25^\circ$ SSH product distributed by the Archiving, Validation, and Interpretation of Satellite Oceanographic data (AVISO) [*Le Traon et al*. 1998; *Ducet et al*. 2000] for 2001–2011 are used to understand ISV of SSH.

To understand the Chl-a variations, 8 day composite surface Chl-a concentrations during 2003–2011 derived from the moderate resolution imaging spectroradiometer (MODIS) sensor on NASA's Aqua satellite [*Justice et al*. 1998] are investigated, together with 8 day composite Sea-viewing Wide Field-of-view Sensor (SeaWiFS) Chl-a concentrations during 2001–2002 from the NASA/Goddard Earth Sciences (GES)/Distributed Active Archive Center (DAAC) [*Aiken et al*., 1995]. The MODIS and SeaWiFS are mapped to spatial resolutions of nearly 5 and 9 km, respectively. Daily satellite-observed outgoing longwave radiation (OLR) from the National Oceanic and Atmospheric Administration [*Liebmann and Smith* 1996] and daily cross-calibrated

Table 1. Summary of HYCOM Experiments[a]

Experiment	Description
NoISO	Remove all ISO effects
NoLOCAL	Remove all ISO effects in SR
NoSWR	Remove ISO SWR
NoWIND	Remove ISO wind speed/stress SWR
NoSTRESS	Remove ISO wind stress

[a]ISO signals in forcing fields are removed with a 105 day lowpass Lanczos filter.

multiplatform (CCMP) satellite ocean surface wind vectors [*Atlas et al*., 2008] are used to investigate tropical deep convection and surface wind associated with atmospheric ISOs from 2001 to 2011.

2.2. Ocean Model and Experiments

The ocean general circulation model used in this study is the HYbrid Coordinate Ocean Model (HYCOM) version 2.2.18, which is configured to the Indian Ocean basin (30°E–122.5°E, 50°S–30°N) with a horizontal resolution of 0.25°×0.25° and 26 vertical layers [*Li et al*., 2014, 2015]. The surface forcing fields include daily 10 m CCMP wind speed and wind stress, 2 m air temperature, and humidity [*Dee et al*., 2011] from the European Center for Medium range Weather Forecasting (ECMWF), surface net SWR and longwave radiation (LWR) from Clouds and the Earth's Radiant Energy System (CERES) [*Wielicki et al*. 1996], and precipitation from Tropical Rainfall Measuring Mission [*Kummerow et al*., 1998]. The surface turbulent heat fluxes (surface latent and sensible heat fluxes) are calculated with the HYCOM simulated SST, together with observed surface wind speed, air temperature, and specific humidity. To focus on examining the effects of forcing over the Indian Ocean, active Indonesian Throughflow is excluded from HYCOM experiments by relaxing the model temperature and salinity to their climatological fields. Further details about the model configuration and forcing fields can be found in *Li et al*. [2014]. This version of HYCOM has been successfully utilized to understand SST variability induced by MJOs [e.g., *Li et al*., 2013, 2014], ISV of sea surface salinity [*Li et al*., 2015], and equatorial wave dynamics over the tropical Indian Ocean [*Chen et al*., 2015].

The model is spun up from a state of rest for 30 years using monthly climatological forcing fields. Restarting from the already spun-up solution, HYCOM is integrated forward from 1 March 2000 to 30 November 2011 with the daily forcing fields described above. This experiment is referred to as HYCOM Main Run (MR). Several parallel experiments are performed with daily atmospheric forcing to isolate effects of different processers (Table 1). To entirely exclude the ISO-related atmospheric variability, all of the atmospheric forcing fields are lowpass filtered with a 105 day Lanczos digital filter [*Duchon*, 1979] in experiment NoISO. The difference, *MR* − *NoISO*, hence measures the overall impact of ISO-related atmospheric forcing on the ocean. The effects of forcing from SWR, wind speed, and wind stress are isolated by performing experiments NoSWR, NoWIND, and NoSTRESS, respectively. In experiment NoSWR, the 105 day lowpass filtered SWR is used. Other forcing fields are the same as those in the MR. The difference, *MR* − *NoSWR*, thus isolates the effect of intraseasonal SWR. In experiment NoWIND, both surface wind speed and wind stress fields are lowpass filtered, and in experiment NoSTRESS only wind stress is lowpass filtered. While surface wind speed affects the ocean through changing turbulent heat fluxes, wind stress affects ocean dynamics (e.g., upwelling due to both remote and local forcing, horizontal advection by currents) and mixed layer process (e.g., entrainment cooling). The difference, *NoSTRESS* − *NoWIND*, measures the effect of wind speed induced turbulent heat fluxes, and *MR* − *NoSTRESS* quantifies the effect of wind stress induced ocean dynamics and entrainment.

While the EIO region in HYCOM experiments is defined as 90°E–120°E, and 15°S–5°N (Figure 1e, dashed-black line enclosed area), a subarea is defined as our Study Region (SR; 95°E–114°E, 10°S–0°N; Figure 1, solid-black line enclosed area) to quantify the upwelling in the EIO. The SR is very similar to the eastern anti-node region of the IOD (90°E–110°E, 10°S–0°N) defined by *Saji et al*. [1999], and it is chosen to cover the prominent negative SSTA and high Chl-a concentration regions in the fall of 2006, when the strongest EIO upwelling event for the 2001–2011 period occurs (Chen et al., submitted manuscript, 2016, Figure 2).

To assess the relative importance of local versus remote forcing on the EIO upwelling, an additional experiment, named as NoLOCAL, is performed, in which all of the atmospheric forcing fields in the SR are 105 day lowpass filtered. The areas between SR and dashed-black lines in Figure 1e mark the transition regions of experiment NoLOCAL, where the realistic daily forcing fields gradually change to no ISV forcing (105 day lowpassed fields) in the SR. The difference, *MR* − *NoLOCAL*, thus isolates the ISO-related local forcing effect, and NoLOCAL measures the remote forcing effect associated with atmospheric ISOs.

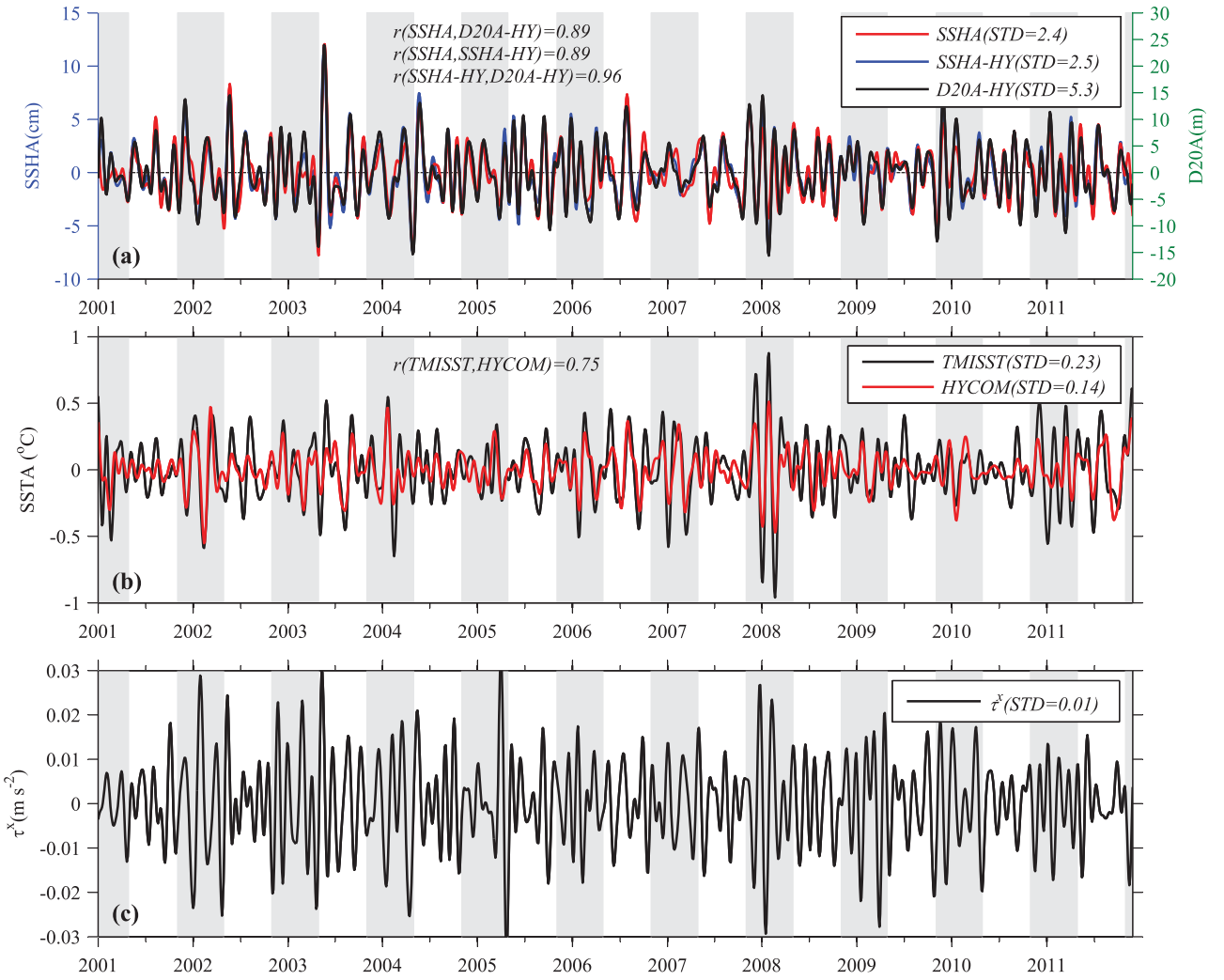

Figure 2. Intraseasonal variability (ISV; 30–105 day band-pass filtered field) averaged in the SR for (a) SSHAs from AVISO (red line) and from HYCOM MR (blue line), and D20A from HYCOM MR (black line); (b) SSTAs from TMISST (black line) and from HYCOM MR (red line). (c) Intraseasonal zonal wind stress, τ^x, averaged in the equatorial Indian Ocean (70°E–100°E, 15°S–15°N). The gray shadings denote the winter-spring season of November–April during 2001–2011.

We focus on analyzing the 3 day averaged model outputs from 2001 to 2011, and the model simulation of 2000 is not used to minimize the transient effect when HYCOM switches its forcing fields from monthly climatology in the spin-up run to realistic daily forcing. In our result analyses, unless specified otherwise all observational and model data are band-pass filtered with a 30–105 day Lanczos digital filter to obtain their intraseasonal components. We also examined the sensitivity of the filtered results to the selection of different cutoff periods of 30–90 days, 30–100 days, and 30–105 days, and obtained similar results (see supporting information Figure S1). Given that ocean response to intraseasonal wind forcing has larger amplitude at lower frequency and obtains a peak response near the 90 day period [*Han et al.*, 2001; *Schouten et al.*, 2002; *Han*, 2005], we choose the 30–105 day periods to fully contain the oceanic intraseasonal signals.

3. Results

3.1. Model/Data Comparison

The performance of HYCOM in the MR has been validated in several recent researches. The HYCOM-simulated mean structures of SST, sea surface salinity (SSS), mixed layer depth (MLD), thermocline depth, and surface circulation over the tropical Indian Ocean agree reasonably well with satellite and in situ

observations [*Li et al*., 2014, 2015]. The simulated zonal currents along the equator also compare favorably with those from mooring observations and from ocean reanalysis data [*Chen et al*. 2015]. In addition, the simulated interannual D20A, SSTA, and SSH anomaly (SSHA) in the EIO agree well with satellite observations and reanalysis data (Chen et al., submitted manuscript, 2016). Here, we only examine the simulated SSHA, D20A, and SSTA on intraseasonal timescales.

The standard deviation (STD) maps of intraseasonal SSHA and SSTA from HYCOM MR in the central and eastern Indian Ocean compare favorably with that observed from AVISO and TMISST (Figure 1). The large-scale patterns and magnitudes of the observed/modeled SSHA agree, albeit with some minor differences (Figures 1a and 1b). Compared with intraseasonal SSTA from TMISST, the intraseasonal SSTA from HYCOM MR is weaker in most regions (Figures 1c and 1d). The STD patterns of observed/simulated SSTAs, however, agree well. The overall larger amplitudes of the observed SSTA from TMISST data likely result from the difference between TMI skin temperature and HYCOM bulk temperature of the top model layer ($\sim$2.6 m in thickness). The skin temperature is more sensitive to surface forcing and therefore obtaining larger variability amplitudes.

To further verify the HYCOM performance in simulating the large-scale ocean ISV in the EIO, we compare the modeled intraseasonal SSHA and SSTA with satellite observations in the SR. The simulated intraseasonal SSHA averaged in the SR shows remarkable agreement with AVISO data, with a correlation coefficient being 0.89 (above the 95% significance level) from 2001 to 2011 (Figure 2a). The STDs of observed and simulated SSHA are 2.4 and 2.5 cm, which also agree well. The intraseasonal D20A from HYCOM MR averaged in the SR is highly correlated with the SSHA from HYCOM MR and AVISO satellite observation. The correlation coefficient is 0.96 between MR D20A and MR SSHA, and 0.89 between MR D20A and AVISO SSHA. Such tight relationship between D20A and SSHA suggests that the dynamical responses of the EIO to ISO atmospheric forcing exhibits a baroclinic structure, with upwelling being associated with an elevated thermocline and lowered sea level. Consistent with Figures 1c and 1d, HYCOM simulated intraseasonal SSTA in the SR has a general agreement with the TMI observed SSTA (Figure 2b), with a correlation coefficient of 0.75 during 2001–2011. As discussed above, the amplitudes of HYCOM SSTAs are systematically weaker than those of TMI SSTAs, due to the difference between TMI skin temperature and HYCOM bulk temperature. The good model/data agreements shown above suggest that HYCOM is able to simulate the observed ISV in the upper Indian Ocean, and therefore can be used to understand the processes that control the EIO upwelling on intraseasonal timescales.

3.2. Intraseasonal Variability of the EIO Upwelling: Forcing by Atmospheric ISOs

As discussed earlier, the EIO upwelling primarily occurs in summer-fall season during May–October, and can be identified by shallow D20 (Figure 3b, dashed curve), low SSH, low SST (Figure 3a, dashed curve), and high Chl-a concentration (Figure 3c, dashed curve). Since large-scale SSHA on intraseasonal timescale generally mirrors D20A (Figure 2a), here we omit SSHA and only show D20A. Evidently, the EIO upwelling—as indicated by D20A and SSTA—exhibits significant ISV, with a STD value of 5.2 m for D20A and 0.11°C for SSTA during summer-fall for 2001–2011 (Figures 3b and 3a). Larger ISV amplitudes, however, often occur in the winter-spring season from November–April (Figures 3a and 3b, solid curves in gray shading areas), when the EIO shows weaker seasonal shoaling of D20 without seasonal SST cooling (Figures 3a and 3b, dashed curves). The STDs of intraseasonal D20A and SSTA are 5.5 m and 0.17°C during winter-spring, which are approximately 60% and 30% of the STDs of their climatological mean seasonal cycles of 9.1 m and 0.57°C for the 2001–2011 period (supporting information Figure S2) and are larger than their magnitudes during summer-fall.

The ISV of D20 averaged in the SR from HYCOM MR agrees very well with that from *MR* − *NoISO*, which isolates atmospheric ISO forcing, with STDs being 5.3 m in the MR and 4.8 m in *MR* − *NoISO*, and correlation coefficient between the MR and *MR* − *NoISO* D20A being 0.96 above 95% significance (Figure 3b). Similarly, intraseasonal SSTAs averaged in the SR from the MR and *MR* − *NoISO* also agree well (Figure 3a), with their correlation coefficient being 0.91 above 95% significance and their STDs being 0.14°C and 0.13°C. These results demonstrate that the ISVs of D20 and SST in the EIO are predominantly caused by atmospheric ISO forcing rather than induced by the oceanic internal instabilities. Because atmospheric ISOs—particularly the dominant mode MJOs—are stronger during November–April in the equatorial Indian Ocean than during

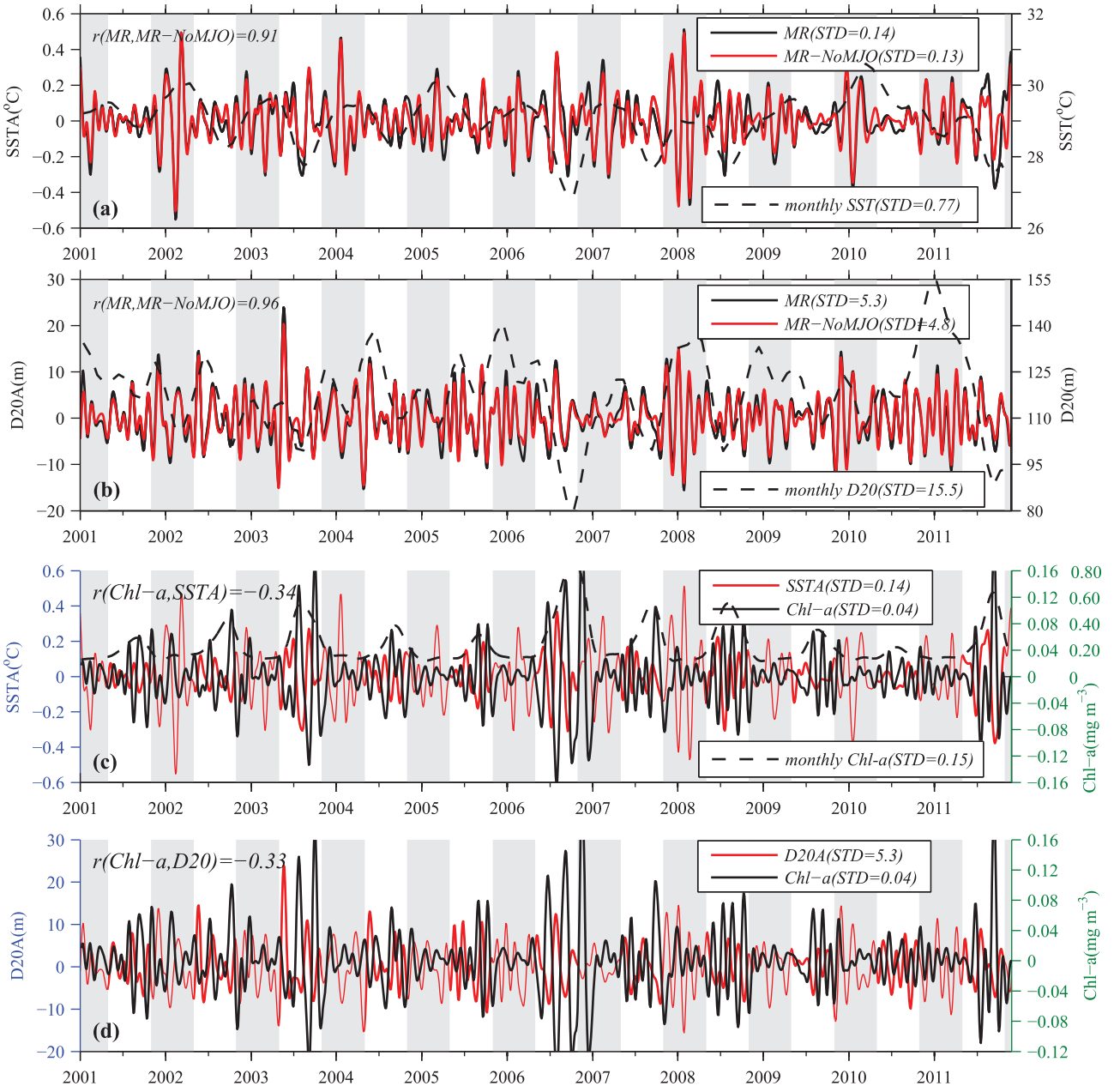

Figure 3. (a) Time series of intraseasonal SSTA averaged in the SR from the MR (black line) and from the solution difference, *MR-NoISO* (red line) for 2001–2011; (b) Same as (a) but for D20A; (c) Intraseasonal SSTA from the MR (red line) and ISV of satellite observed Chl-a concentration (black line) averaged in the SR; (d) Same as (c) but for MR D20A and observed Chl-a. Monthly modeled SST, D20, and observed Chl-a averaged in the SR are also shown by dashed-black curves in Figures 3a–c, respectively. Intraseasonal variability of Chl-a and monthly Chl-a in Figure 3c range from −0.16 to 0.16 mg m^{-3} and 0–0.80 mg m^{-3}, and they are labeled on the right.

May–October (Figure 2c) [see *Zhang*, 2005 for a review], they force larger amplitude ISVs of D20, SSH, and SST in the upper ocean during winter season.

Interestingly, even though intraseasonal D20A and SSTA over the EIO generally obtain larger amplitudes during winter-spring, anomalies of Chl-a concentration have apparently larger amplitudes during the summer-fall upwelling season (Figures 3c and 3d, solid black line), with a STD of 0.05 mg m^{-3} during May–October of 2001–2011, which is ~46% of its climatological mean seasonal cycle (STD = 0.11 mg m^{-3}). The intraseasonal Chl-a anomalies show negative correlations with intraseasonal SSTA and D20A when all seasons are considered, with correlation coefficients being −0.34 and −0.33, respectively. When only the summer-fall season is considered, the cross correlation coefficient between Chl-a and SSTA increases to −0.55, and that between Chl-a and D20A increases to −0.51. High Chl-a corresponds to low SSTA and

shallow D20A associated with intensified upwelling, and low Chl-a corresponds to high SSTA and deep D20A associated with reduced upwelling. These situations are particularly clear during 2003, 2006, 2008, and 2011 (Figures 3c and 3d), when D20 is anomalously shallow and SST is anomalously cold on interannual timescales (Figures 3b and 3a, dashed curves). Although intraseasonal D20A and SSTA have larger amplitudes during winter-spring, they have no statistically significant correlation with Chl-a anomalies (−0.09 and −0.12) for this season. For some years (e.g., 2002 and 2003), however, significant intraseasonal Chl-a blooms occur even during winter-spring, with Chl-a anomalies exceeding 0.05 mg m^{-3}.

Note that intraseasonal D20A is not significantly correlated with intraseasonal SSTA in the EIO when all seasons are included, with a correlation coefficient of only −0.17 for the SR during 2001–2011. The correlation map between SSTA and D20A, however, shows that larger correlation coefficients of ∼0.3 (Figure 1e) can occur in areas of the EIO where the mean thermocline is relatively shallow (Figure 1f). As shown in supporting information Figure S2, the climatological mean D20 averaged in the SR is shallower during summer-fall with the minimum value of 103 m occurring in September, but it is deeper in winter-spring with a minimum depth of 115 m. The intraseasonal SSTA/D20A correlation reaches the maximum of 0.48 in summer-fall when D20A leads by 8 days, and the maximum of −0.51 in winter-spring when SSTA leads by 3 days. These results suggest that D20A affects SSTA during summer-fall upwelling season, but has little contribution to SSTA in winter-spring (see section 3.4 for details).

The obvious seasonality of ISV between summer-fall and winter-spring is related to the different mean thermocline depth over the EIO. Since the EIO SR is located within the Indian Ocean side of the Indo-Pacific warm pool, the mean thermocline is generally deep especially during winter-spring (supporting information Figure S2). Thus, even if the thermocline shoals significantly in winter-spring on intraseasonal timescales, it is often not strong enough to efficiently affect SST and Chl-a. By contrast, during summer-fall, the thermocline is shallower and intraseasonal perturbations in D20 can more effectively affect SST and Chl-a. *Kawamiya and Oschlies* [2001] and *Iskandar et al*. [2010] also showed that low SST and shallow D20 are not always associated with high surface Chl-a concentration, and concluded that the enhancement of surface Chl-a occurs only if the deep chlorophyll maximum gets into contact with the surface mixed layer.

3.3. Remote Versus Local Forcing

Lagged correlation analyses between intraseasonal wind stress anomaly at each grid and intraseasonal D20A averaged in the SR demonstrate that ISV of D20 in the EIO is affected by both local and remote wind stress not only in summer-fall (Figures 4a and 4b), but also in winter-spring (Figures 5a and 5b). The higher positive correlation coefficients with zonal wind stress in the equatorial ocean, together with the apparent eastward propagation of the correlation maxima (Figures 4a and 5a), suggest that remote forcing by zonal wind in the equatorial Indian Ocean is an important factor that causes intraseasonal D20A in the EIO. Intraseasonal easterly (westerly) wind anomalies along the equator act to shoal (deepen) D20, and the anomalous D20 signals propagate eastward as equatorial Kelvin waves, enhancing (weakening) the EIO seasonal-to-interannual upwelling. The lagged correlation, especially when zonal wind stress leads D20A by 15 days and 10 days (Figures 4a and 5a), is due to the propagation time of equatorial Kelvin waves from the equatorial Indian Ocean to the SR region. The southerly winds near the coasts of Sumatra and Java have negative correlations with D20A (Figures 4b and 5b), suggesting the importance of local meridional winds in causing EIO upwelling. Evidently, remote influence of winds on D20A results primarily from zonal wind component along the equator, with meridional wind effects being largely local to the EIO upwelling region.

Similarly, intraseasonal SSTA averaged in the SR during summer-fall is also positively (negatively) correlated with zonal (meridional) wind stress in the eastern equatorial Indian Ocean (local to the EIO), with lower correlation coefficients in comparison to those of D20A (Figures 4c and 4d). The zonal wind stress that affects the EIO SSTA, however, appears to be more confined to the eastern equatorial basin comparing to the zonal wind that remotely affects EIO D20A (compare Figures 4a and 4c). This is because the intraseasonal SSTA is dominated by upwelling during summer-fall (see section 3.4). Since it takes the D20A another week to affect SSTA (section 3.4), the correlation pattern between τ^x and SSTA extends further west when wind leads by 25 days (−25 d; figure not shown). By contrast, during winter-spring intraseasonal SSTA averaged in the SR is negatively correlated with local zonal wind stress (Figure 5c) and positively correlated with local meridional wind stress (Figure 5d). These results suggest that wind stress is not the main cause for the EIO intraseasonal SSTA during this season, because easterly (southerly) wind stress is upwelling favorable and thus

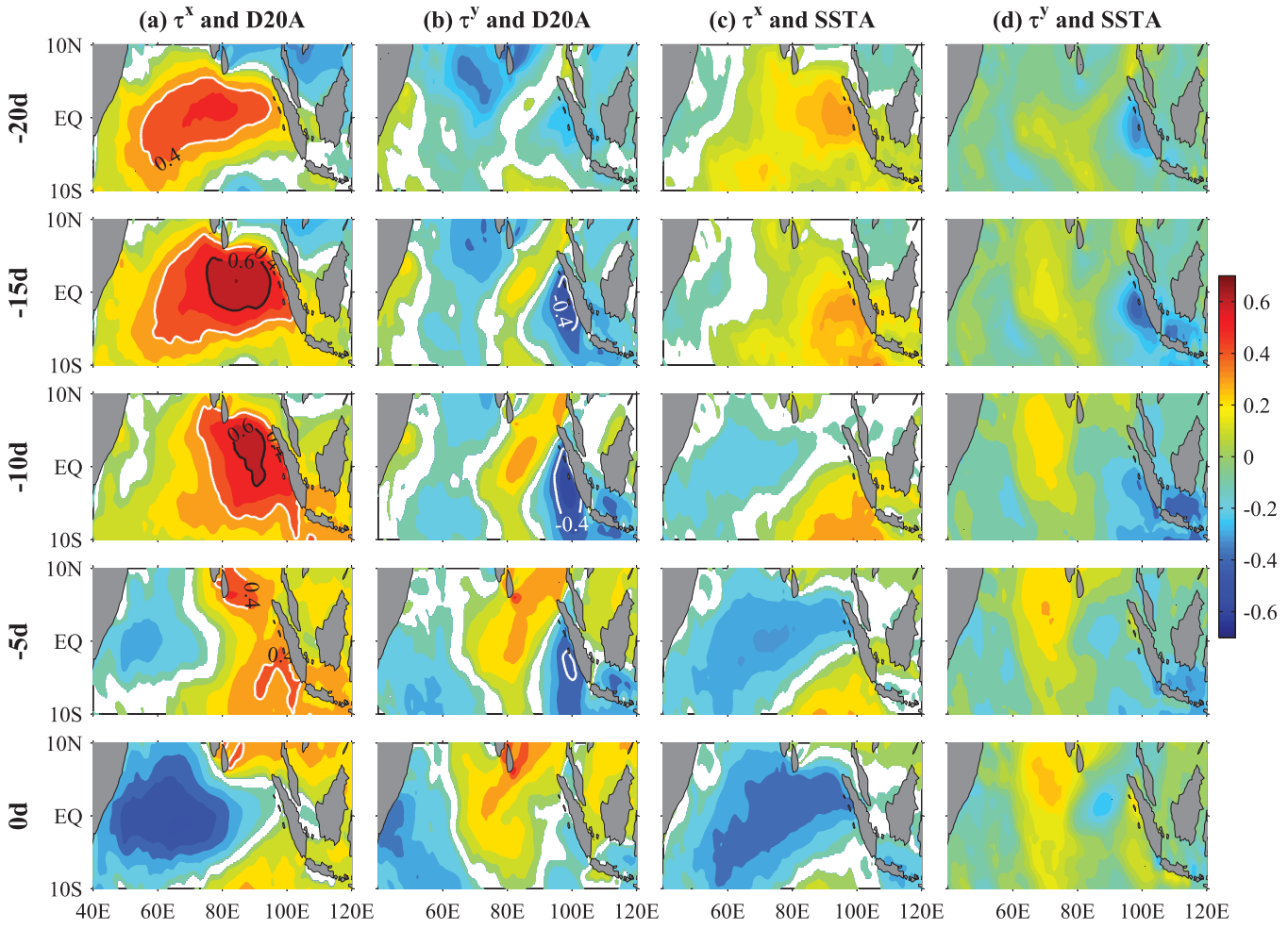

Figure 4. (a) Correlation coefficients between intraseasonal zonal wind stress (τ^x) at each grid point and intraseasonal D20A averaged in the SR from the MR in summer-fall (May–October) when τ^x leads D20A by 20, 15, 10, 5, and 0 days. Only grid points with confidence levels above 95% are plotted. (b) Same as Figure 4a but for meridional wind stress (τ^y) and D20A. (c) Same as Figure 4a but for τ^x and SSTA. (d) Same as Figure 4a but for τ^y and SSTA.

should be positively (negatively) correlated with the SSTA. Comparing to D20A, intraseasonal SSTA in the EIO is less associated with remote forcing from the equator.

In addition to surface wind stress, we also examined the correlations between surface wind stress curl and wind speed anomalies with D20A and SSTA (supporting information Figures S3 and S4). During summer-fall, the EIO D20A is significantly correlated with wind stress curl anomaly near the Sumatra and Java coasts with correlation coefficients being larger than 0.4, and to a lesser degree, SSTA is also positively correlated with wind stress curl anomaly during this season (supporting information Figures S3a and S3b). These results indicate that anomalous negative (positive) wind stress curl, which corresponds to positive (negative) Ekman Pumping velocity south of the equator, contributes to the coastal upwelling anomaly, because negative (positive) wind stress curl anomaly is divergence and upwelling (convergence and downwelling) favorable, and thus should be positively correlated D20A and SSTA. On the other hand, during winter-spring the EIO SSTA is correlated negatively with wind stress curl anomaly near the Sumatra and Java coasts, with correlation coefficient magnitudes being larger than 0.4. This result indicates that the local wind stress curl anomaly acts to damp the intraseasonal SSTA induced by other processes. For example, positive (negative) wind speed anomaly increases (decreases) surface turbulent heat flux loss and thus cools (warms) the SST. Indeed, negative correlations between the SR SSTA and local wind speed anomaly are found during winter-spring, demonstrating that surface turbulent heat flux induced by local wind speed plays an important role in the EIO SSTA variations during winter-spring but not during summer-fall (supporting information Figure S4).

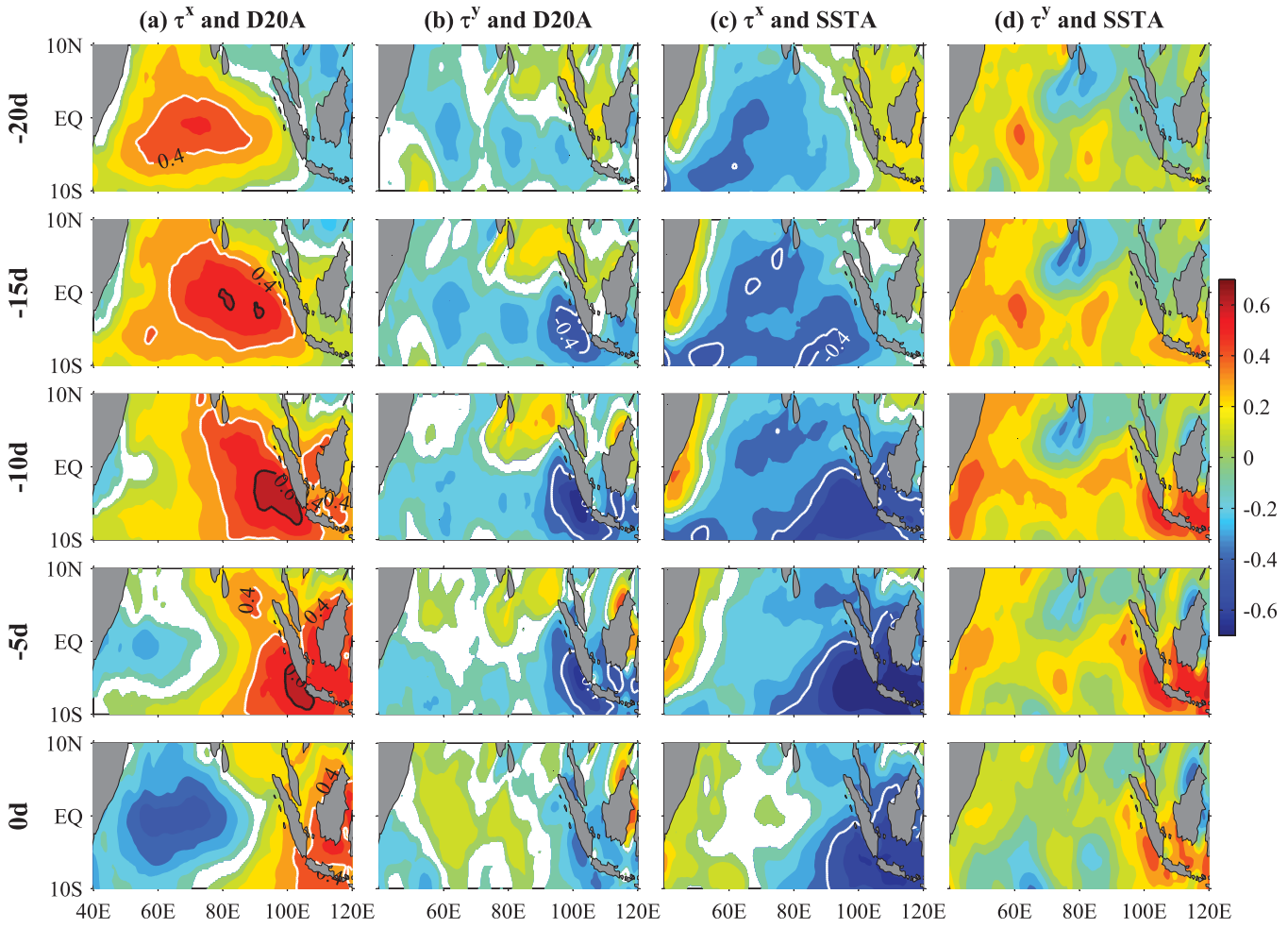

Figure 5. Same as Figure 4 but for winter-spring (November–April).

To confirm the above empirical analysis and quantify the remote versus local wind forcing effects, we obtain the time series of intraseasonal D20A in the SR from the MR and NoLOCAL experiments (Figure 6a). The correlation coefficient between D20A from the MR and from experiment NoLOCAL (*MR* − *NoLOCAL*) is 0.95 (0.67). The STD of D20A during 2001–2011 is 5.3 m in MR, 4.3 m in NoLOCAL (remote forcing effect), and 1.8 m in *MR* − *NoLOCAL* (local forcing effect), with the STD of remotely forced D20A being 81% of the total D20A (STD(*NoLOCAL*)/STD(MR) = 0.81) and that of locally forced D20A being 34% of the total D20A (STD(*MR*− *NoLOCAL*)/STD(MR) = 0.34). Note that the contributions of local and remote forcing to the MR STD do not add up to 1, because of the nonlinearity of STD calculation formula. Remote forcing by equatorial winds dominates the MR D20A in the EIO during most of the time, and local wind forcing in the EIO is less important. For some years, however, local forcing is as important as remote effect particularly during winter-spring due to the stronger intraseasonal wind stress induced by the MJO (see section 3.4).

Comparing to D20A, SSTA off the Sumatra and Java coasts results predominantly from local forcing (Figure 6b). The STD of SSTA is 0.14°C for the MR, 0.08°C for *NoLOCAL*, and 0.12°C for *MR*− *NoLOCAL* during 2001–2011, and correlation coefficient between MR and NoLOCAL (*MR*− *NoLOCAL*) SSTA is 0.49 (0.85). The intraseasonal SSTA is essentially controlled by local forcing in winter-spring, but is also contributed by remote forcing in summer-fall especially for 2003, 2006, 2008, and 2011 (Figure 6b) when the mean thermocline is shallow (Figure 3b, dashed curve). As mentioned earlier, during the summer-fall season of the 4 years, high (low) Chl-a concentration corresponds to shallow (deep) D20A and cold (warm) SSTA (Figure 3). This is because remote forcing from the equator affects D20A and thus SSTA and Chl-a.

To further support the above arguments, we examine the time-longitude plots of intraseasonal anomaly of surface wind stress, intraseasonal D20A and SSTA along the equator (from 50°E to location B of Figure 1e,

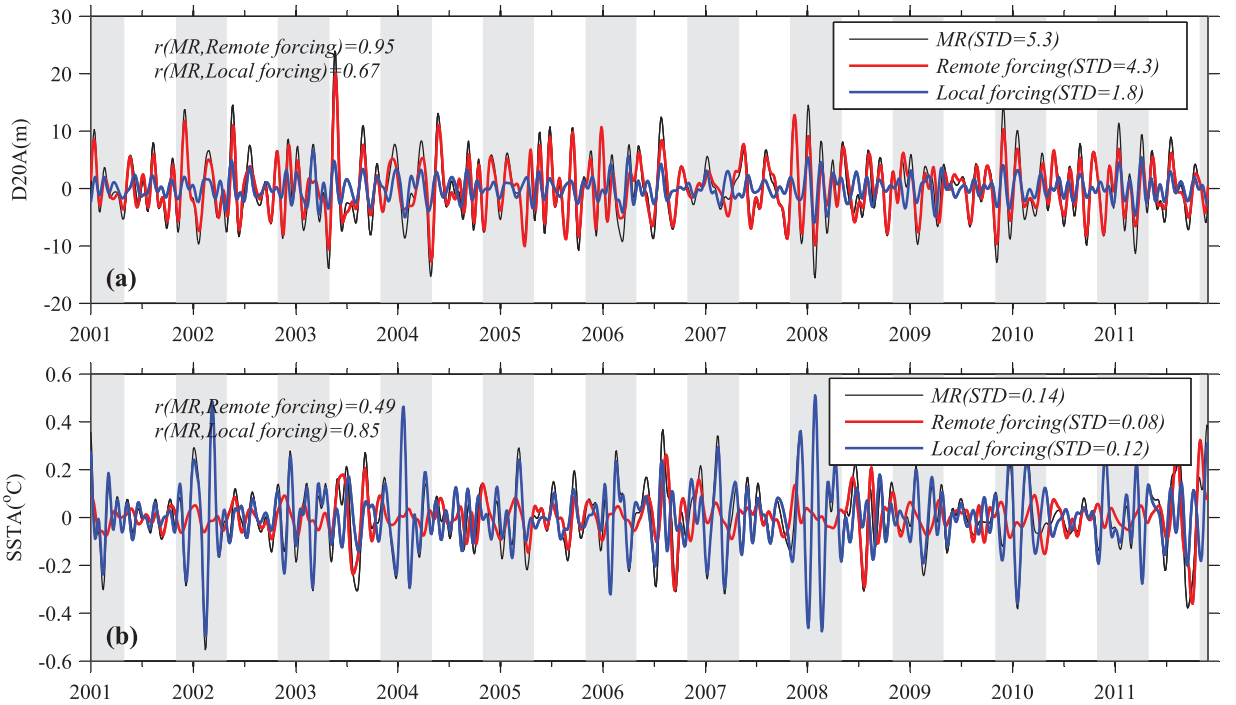

Figure 6. (a) Intraseasonal D20A averaged in the SR from solution MR (black line), experiment NoLOCAL (red line), and *MR − NoLOCAL* (blue line). (b) Same as Figure 6a but for SSTA.

which is at 98.5°E) and along the coasts of Sumatra and Java (Figure 1e, from locations B to D, the red line) from HYCOM MR (the complete solution), experiment NoLOCAL that measures remote forcing effect, and their difference *MR-NoLOCAL* that estimates the local forcing effect (Figure 7). Due to the similar contribution features about remote and local forcing to the EIO upwelling from 2001 to 2011, we only show the results of 2001–2002 below to further reveal the remotely forced wave process versus local contribution. Evidently, intraseasonal D20A along the EIO coasts (from B to D) is dominated by remote forcing from the equator (compare Figures 7b–7d), with D20A generated by equatorial winds (Figure 7a) propagating eastward along the equator and then southeastward along the Sumatra-Java coasts (Figure 7b). The intraseasonal D20A in experiment NoLOCAL presents similar magnitude and propagation features to that in HYCOM MR, suggesting that remotely forced Kelvin waves are the major cause for the intraseasonal D20A in the EIO (compare Figures 7b and 7c). Local forcing however can also have significant contributions during some years, such as during the winter-spring season of 2002 (Figure 7d). In comparison to intraseasonal D20A, the propagation of intraseasonal SSTA is less apparent (Figure 7e), and SSTA off Sumatra and Java coasts results predominantly from local forcing (Figures 7e–7g).

3.4. EIO Intraseasonal SSTA: Controlling Processes

In the tropical Indian Ocean, ISOs induce intraseasonal SST variability mainly through SWR, surface turbulent heat fluxes associated with wind speed variation, and wind stress-driven oceanic processes [e.g., *Shinoda and Hendon* 1998; *Waliser et al*., 2003, 2004; *Saji et al*. 2006; *Han et al*., 2007; *Vinayachandran and Saji*, 2008; *Jayakumar et al*., 2011; *Vinayachandran et al*., 2012; *McPhaden and Foltz*, 2013; *Li et al*., 2014]. The relative importance of the three however shows large spatial and temporal variations. To assess the effects of different processes on SSTA in the equatorial EIO, we analyze intraseasonal SSTA induced by SWR (*MR − NoSWR*), turbulent heat flux associated with wind speed variation (*NoSTRESS − NoWIND*), and wind stress driven oceanic processes (*MR − NoSTRESS*) (Figure 8). The STDs of the three forcing factors have comparable magnitudes of 0.08°C, 0.07°C, and 0.06°C, and their correlation coefficients with the MR SSTA are 0.69, 0.67, and 0.48, respectively, when all seasons are considered. Overall, SWR plays a slightly larger role than turbulent heat fluxes induced by wind speed and oceanic processes (e.g., upwelling, horizontal advection, and entrainment) induced by intraseasonal wind stress, with the contribution from the oceanic processes being the weakest, even though its effect is still comparable with the other two.

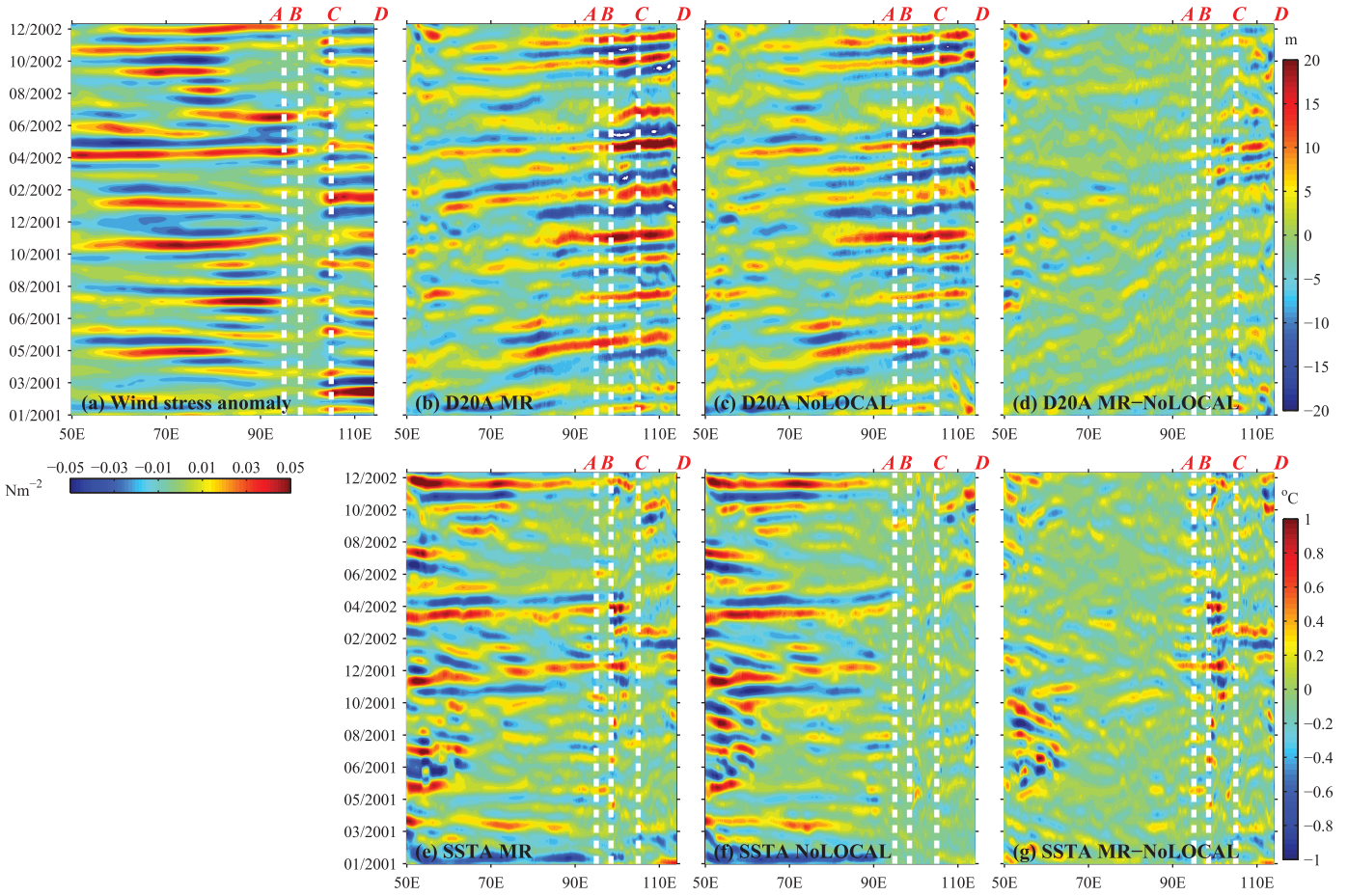

Figure 7. (a) Time longitude plot of intraseasonal (30–105 day band-pass filtered) zonal wind stress along the equator and wind stress component along the red line (from B-to-D) shown in Figure 1e; Values between 50°E and B represent zonal wind stress along the equator with positive eastward, and those from B to D represent wind stress along the coasts with positive southeastward; the longitude of locations A, B, C, and D are 95°E, 98.5°E, 105°E, and 114°E, respectively; (b)–(d) are the same as Figure 7a but for D20A from Figure 7b the MR, Figure 7c experiment NoLOCAL that isolates remote forcing, and Figure 7d their difference *MR − NoLOCAL* that assesses the local forcing within the EIO; (e)-(g) are the same as Figures 7b–d but for SSTA from HYCOM experiments.

When only the winter-spring is considered, SWR becomes more important. The STD of SSTA in winter-spring induced by SWR is 0.10°C compared to 0.17°C in the MR, which is ∼59% of the MR STD, comparing to the 0.09°C (∼53%) induced by wind speed and 0.06°C (∼35%) induced by wind stress. The correlation coefficient between SSTA in the MR and SSTA induced by SWR is 0.88, which is larger than the 0.78 due to wind speed and 0.39 due to wind stress. During summer-fall, however, SWR contributes much less to intraseasonal SSTA in the equatorial EIO, and wind stress is the largest contributor to the SSTA. The STD of SSTA in the MR is 0.11°C, and that from the effects of SWR, wind speed and wind stress are 0.05°C, 0.05°C, 0.07°C, which are ∼45%, ∼45%, and ∼64% of the MR STD, respectively. The correlation coefficients between the MR SSTA and that forced by SWR, wind speed, and wind stress are respectively 0.10, 0.38, and 0.63.

To further illustrate the processes that control intraseasonal SSTA in the equatorial EIO, we perform composite analyses for cold and warm intraseasonal SSTA events during summer-fall and winter-spring seasons. The ±1.5 STD of SSTA from the MR for the 2001–2011 period is ±0.21°C, which is used to identify warm and cold SSTA events. Based on these criteria, we identify 5 summer-fall and 13 winter-spring cold SSTA events, and 4 summer-fall and 12 winter-spring warm events (Figure 8a) for our composite analyses (Figure 9). The days with SSTA minima (maxima) are taken as day 0. Then, SSTA composites for 20 days before (day −20) and 20 days after (day +20) day 0 are obtained.

Wind stress dominates the SSTA of the cold events during summer-fall, with SWR and turbulent heat flux associated with wind speed contributing significantly less (Figure 9a). During the peak of the cold SSTA, D20A shoals (negative; Figure 9b), Chl-a blooms (Figure 9d), with both D20A and Chl-a peaks leading the

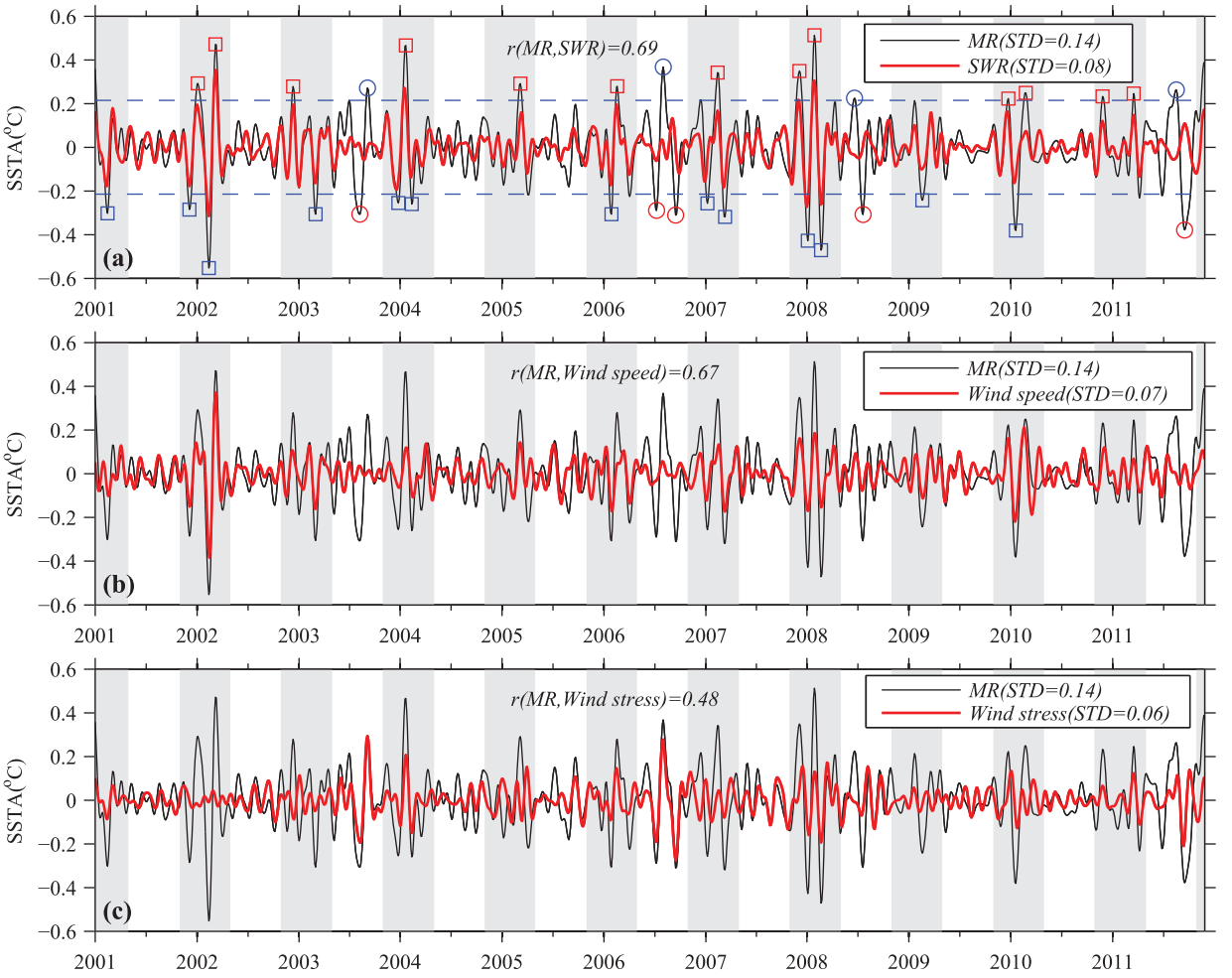

Figure 8. (a) Intraseasonal SSTA averaged in the SR from HYCOM MR (black line) and *MR-NoSWR* solution (red line; SWR effect); the dashed blue horizontal lines show ±1.5 STDs of SSTA from the MR; the blue squares (red circles) mark the SSTA minima with magnitudes exceeding −1.5STD during winter-spring (summer-fall) season, which is identified as cold SSTA events for the respective season; and the red squares (blue circles) mark the SSTA maxima with magnitudes exceeding +1.5 STD in winter-spring (summer-fall) season, which is identified as warm SSTA events for the respective season; (b) Same as Figure 8a but for SSTA from the MR and the *NoSTRESS − NoWIND* solution (turbulent heat flux associated with wind speed effect); (c) Same as Figure 8a but for SSTA from the MR and *MR − NoSTRESS* solution (ocean dynamics and mixed layer physics (e.g., entrainment) induced by intraseasonal wind stress).

SSTA peak by ~8 days. This result suggests that the upwelling process, which is accompanied by high Chl-a, needs approximately a week to significantly affect the SSTA. Note that Chl-a data are available for every 8 days (section 2.1) and HYCOM D20A results (section 2.2) are the 3 day mean values, the slight difference in time lag for Chl-a/SSTA and D20A/SSTA likely result from their difference in resolution. While upwelling tends to thin the surface mixed layer, entrainment tends to thicken the mixed layer. Given that the MLD anomaly thins (Figure 9c) along with the shoaling D20A, upwelling rather than entrainment is the dominant process that causes the cold SSTA. As D20A (upwelling) is controlled by remote forcing (Figure 9b), remote equatorial wind stress dominates the cold SSTA events in the EIO (Figure 9g). The composite wind stress is northwestward (southeasterly) in the equatorial EIO and thus is upwelling favorable (vectors in Figure 10a). Surface wind anomalies converge to the enhanced convection (negative OLR) and diverge from the weakened convection (positive OLR) regions, forming the anomalous southeasterlies in the eastern equatorial basin. Likewise, the warm SSTA events during summer-fall (Figures 9o–9u) are accompanied by the deepened D20A and negative Chl-a anomaly, and are dominated by the downwelling induced by northwesterly wind stress anomaly (Figures 9p–9u and 10c). Remote forcing plays a more important role than local forcing in determining intraseasonal SSTA (Figure 9u).

Different from the summer-fall season, the cold (warm) SSTA events in winter-spring show an out-of-phase relationship between SSTA and D20A (Figures 9h–9i and 9v–9w). Instraseasonal SWR and wind speed are the first and second important factors for causing intraseasonal SSTA, with less contribution from wind stress induced

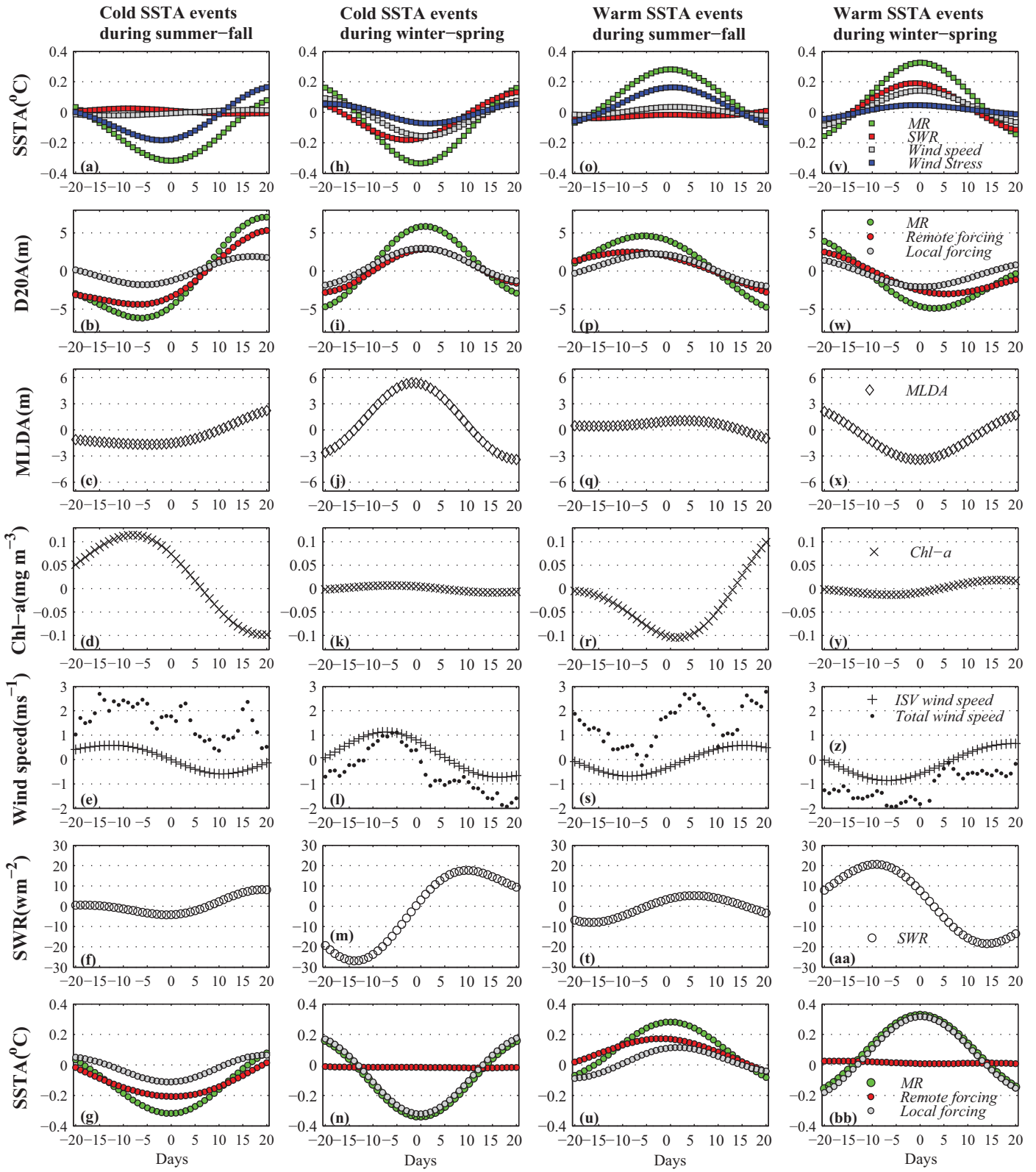

Figure 9. (first column) Composite for the cold SSTA events in summer-fall for (a) intraseasonal SSTA from the MR, *MR-NoSWR* (SWR effect), *NoSTRESS − NoWIND* (wind speed effect), and *MR − NoSTRESS* (wind stress effect) solution; (b) intraseasonal D20A from the MR, NoLOCAL, and the *MR-NoLOCAL* solution; (c) intraseasonal mixed layer depth anomaly; (d) intraseasonal Chl-a anomaly; (e) intraseasonal (black pluses) and total (black dots) wind speed anomalies; (f) intraseasonal SWR anomaly; and (g) intraseasonal SSTA from MR, NoLOCAL, and the *MR-NoLOCAL* solution. (second column) Same as the first column but for the cold SSTA events in winter-spring. (third column) Same as the first column but for the warm SSTA events in summer-fall. (Forth column) Same as the first column but for the warm SSTA events in winter-spring. All variables are averaged in the SR.

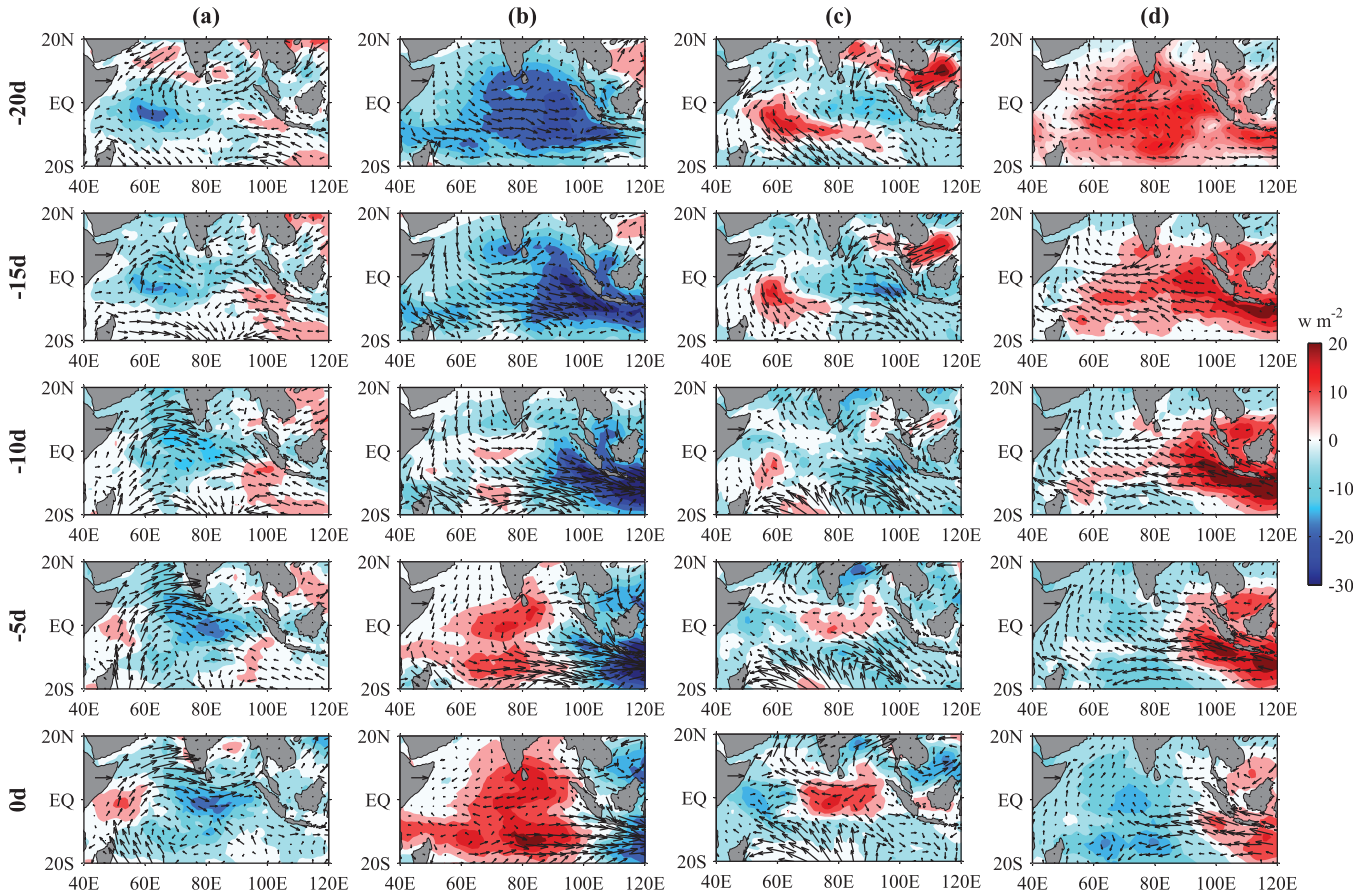

Figure 10. (a) Intraseasonal wind stress (arrows; N m^{-2}) and OLR (color; W m^{-2}) for the composite of cold SSTA events during summer-fall, with a 5 day interval with respect to day 0, the peak date of cold SSTA; The scale in top left corner of each plot represents 0.02 N m^{-2}; (b) Same as Figure 10a but for cold SSTA events in winter-spring; (c) Same as Figure 10a but for warm SSTA events in summer-fall; (d) Same as Figure 10a but for warm SSTA events in winter-spring.

oceanic processes (Figures 9h and 9v). The decreased (increased) SWR (Figures 9m and 9aa) associated with positive (negative) phases of atmospheric ISOs (Figures 10b and 10d) cools (warms) the equatorial EIO, and contribute the most to the EIO intraseasonal SSTA (Figures 9h and 9v, red squares). Meanwhile, the northwesterly (southeasterly) wind anomalies associated with the convective (suppressed) phase of atmospheric ISOs (Figures 10b and 10d) act to intensify (weaken) the winter-spring mean winds in the equatorial EIO (Figure 11a),

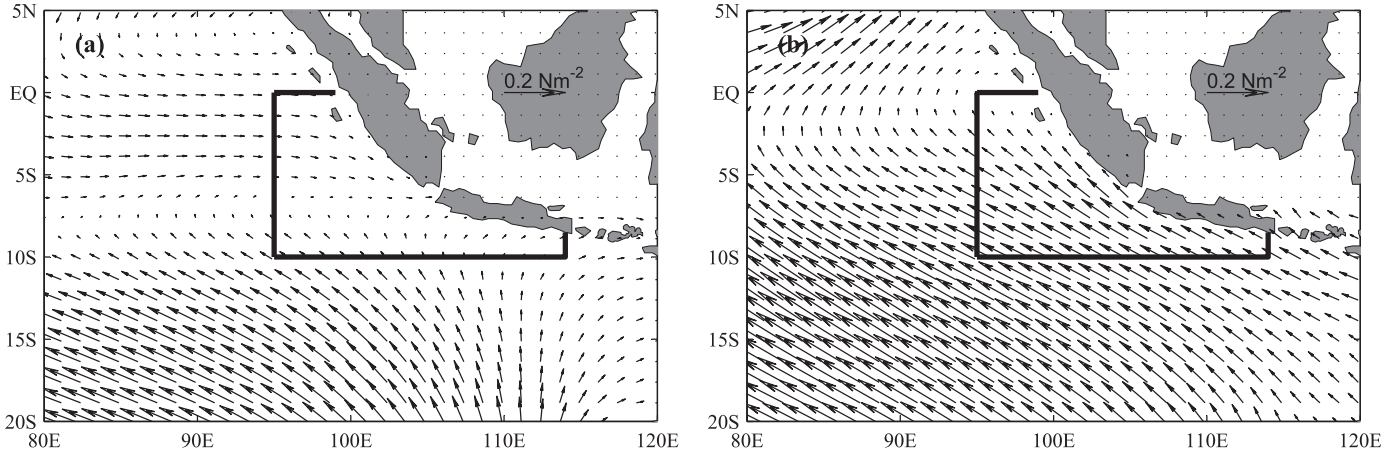

Figure 11. CCMP surface wind stress (in N m^{-2}) for (a) November–April (winter–spring) mean and (b) May–October (summer-fall) mean during 2001–2011.

increasing (decreasing) the total wind speed there (Figures 9l and 9z), and thus cooling (warming) the EIO (Figures 9h and 9v). Furthermore, the reduced (increased) SWR and intensified (weakened) surface wind speed tend to destabilize (stabilize) oceanic stratification and thus thicken (thin) the mixed layer (Figures 9j and 9x), increasing (reducing) the entrainment cooling and thus cooling (warming) the SST. Although D20 shows stronger ISV during winter-spring (e.g. Figure 3b), it has less impact on SSTA and Chl-a due to the deeper mean thermocline. The SSTA is thus almost entirely controlled by local forcing (Figures 9n and 9bb).

4. Summary and Discussion

The equatorial EIO upwelling cools SST in the Indian Ocean side of the Indo-Pacific warm pool, and thus contributes to anomalous atmospheric circulation and impacts regional and global climate. In this paper, we combine observational analyses using satellite data and modeling experiments using HYCOM to investigate the physical processes that determine intraseasonal variability of the EIO upwelling. Specifically, we examine intraseasonal D20A, SSHA, SSTA, and Chl-a, which can all signify upwelling, and quantify the influences of remote forcing from the equator and local forcing within the EIO.

Subject to strong forcing by atmospheric ISOs, the summer-fall (May–October) EIO upwelling—as indicated by D20A, SSHA, and SSTA—exhibits significant ISV (Figures 2a, 2b, 3a, and 3b). Since SSHA mirrors D20A (Figure 2a), we primarily discuss D20A. The STD values are 5.2 m for D20A and 0.11°C for SSTA during May–October from 2001 to 2011. Larger oceanic ISV amplitudes occur during winter-spring (November–April), when atmospheric ISOs—particularly the MJO—are stronger than summer-fall (Figures 3a and 3b). The STD values are 5.5 m for D20A and 0.17°C for SSTA for this season, which are approximately 60% and 30% of the STDs of their climatological mean seasonal cycles.

Although intraseasonal D20A and SSTA over the EIO generally obtain larger amplitudes during winter-spring, the Chl-a concentration obtains its largest intraseasonal variability during summer-fall (Figure 3c), with a STD of 0.05 mg m^{-3} during May–October of 2001–2011, which is ~46% of its climatological mean seasonal cycle. Intraseasonal D20A is significantly correlated with intraseasonal SSTA ($r = 0.48$) and Chl-a ($r = -0.51$) during summer-fall, but is negative correlation with SSTA and Chl-a during winter-spring (Figures 3c and 3d). The obvious seasonality of Chl-a concentration and relationship among intraseasonal D20A, SSTA, and Chl-a result from the different mean thermocline depth over the EIO. Intraseasonal D20A can effectively affect SST and Chl-a during summer-fall when the mean thermocline is shallower, but is often not strong enough to efficiently affect SST and Chl-a during winter-spring when the mean thermocline is generally deep.

During summer-fall, remote forcing by equatorial wind stress plays a dominated role in causing EIO intraseasonal upwelling (Figures 4 and 6a). The STD of D20A in the EIO is 5.2 m in HYCOM MR, 4.4 m in NoLOCAL that estimates the remote forcing but only 1.5 m in *MR − NoLOCAL* that measures local forcing during May–October of 2001–2011. Driven by the equatorial Indian Ocean zonal wind stress, the intraseasonal D20A signals propagate eastward along the equator as equatorial Kelvin waves and southeastward along the coasts of Sumatra and Java as coastal Kelvin waves (Figures 7a–7d). The remote equatorial wind stress dominates the ISV of D20, and controls the ISV of SST and Chl-a in the EIO with a shallower mean thermocline.

During winter-spring, although remote forcing by equatorial wind is still the major cause for intraseasonal D20A in the EIO (Figures 5 and 6a), local forcing is as important as remote effect for some events (Figure 9) due to the strong intraseasonal wind stress induced by the MJO within the EIO. Because of the deep thermocline, intraseasonal D20A has less impact on SSTA and Chl-a. During this season, the SSTA is almost entirely controlled by local forcing. Intraseasonal SWR and wind-speed induced turbulent heat flux are the first and second important factors for inducing intraseasonal SSTA. The decreased (increased) SWR and increased (decreased) wind speed associated with the convective (suppressed) phase of atmospheric ISOs cool (warm) the equatorial EIO, and thus contribute the most to the EIO intraseasonal SSTA (Figures 9–11). Low Chl-a concentration appears in winter-spring (Figure 3c), and the STD of Chl-a during November–April of 2001–2011 is only 0.03 mg m^{-3} on intraseasonal timescales.

Interestingly, significant intraseasonal Chl-a blooms occur even during winter-spring for 2002 and 2003, with Chl-a anomalies exceeding 0.06 mg m^{-3} around 26 January 2002 and 0.05 mg m^{-3} around 25 December 2002, respectively (Figure 3c). During the peak of the Chl-a in January 2002, the D20A shoals by 9.7 m,

with its peak leading the Chl-a peak by ~5 days. Remote forcing dominates the intraseasonal D20A during this event and contributes 76% of the D20A. By contrast, D20A shoals only by 2.6 m in December 2003, which leads Chl-a by 2 days, and it is mainly controlled by the local forcing (91%). Both events correspond to a shallower thermocline (Figure 3b), especially in January 2002 when D20 is only 104 m. These results demonstrate that both remote and local intraseasonal forcing could induce Chl-a bloom in winter-spring if the thermocline is shallow on interannual timescales.

Acknowledgments

TMISST data are produced by Remote Sensing Systems and sponsored by the NASA Earth Sciences Program. Data are available at www.remss.com. The altimeter data were obtained at http://www.aviso.oceanobs.com/en/data.html, the OLR data at http://www.esrl.noaa.gov/psd/data/gridded/data.olrcdr.interp.html, the CCMP wind at http://dx.doi.org/10.5067/CCF30-01XXX, the MODIS Chl-a at http://modis.gsfc.nasa.gov/data/dataprod/chlor_a.php, and the SeaWiFS Chl-a at http://oceancolor.gsfc.nasa.gov/cms/. Gengxin Chen is supported by the "Strategic Priority Research Program" of the Chinese Academy of Sciences (grants XDA11010103 and XDA11010302), National Natural Science Foundation of China (grants 41476011, 41521005, 41476012, and 41206008), and Pearl River S&T Nova Program of Guangzhou (2013J2200087). Weiqing Han and Yuanlong Li are supported by NSF Climate and Large-Scale Dynamics award 1446480 and NOAA award NA11OAR4310100. Dongxiao Wang is support by the CAS/SAFEA International Partnership Program for Creative Research Teams, and the External Cooperation Program of BIC, CAS (grant GJHZ201319). Toshiaki Shinoda is supported by NOAA grant NA150AR431074 and NSF grant AGS-1347132.

References

Aiken, J., G. F. Moore, C. C. Trees, S. B. Hooker, and D. K. Clark (1995), The SeaWiFS CZCS-Type Pigment Algorithm, in *SeaWiFS Technical Report Series, vol. 29, NASA Tech. Memo. 104566*, edited by S. B. Hooker and E. R. Firestone, 34 pp., NASA Goddard Space Flight Cent., Greenbelt, Md.

Atlas, R., J. Ardizzone, and R. N. Hoffman (2008), Application of satellite surface wind data to ocean wind analysis, *Proc. SPIE Int. Soc. Opt. Eng.*, *7087*, doi:10.1117/12.795371.

Chen, G., W. Han, Y. Li, D. Wang, and M. J. McPhaden (2015), Seasonal-to-interannual time scale dynamics of the equatorial undercurrent in the Indian ocean, *J. Phys. Oceanogr.*, *45*, 1532–1553.

Chen, G., W. Han, Y. Li, and D. Wang (2016), Interannual Variability of Eastern Indian Ocean Upwelling: Local versus Remote Forcing, *J. Phys Oceanogr.*, in 2nd review.

Dee, D. P., et al. (2011), The ERA-Interim reanalysis: Configuration and performance of the data assimilation system, *Q. J. R. Meteorol. Soc.*, *137*(656), 553–597.

Ducet, N., P. Y. Le Traon, and G. Reverdin (2000), Global high-resolution mapping of ocean circulation from TOPEX/Poseidon and ERS-1 and-2, *J. Geophys. Res.*, *105*(C8), 19,477–19,498.

Duchon, C. E. (1979), Lanczos filtering in one and two dimensions, *J. Appl. Meteorol.*, *18*(8), 1016–1022.

Han, W.(2005), Origins and dynamics of the 90-day and 30–60-day variations in the equatorial Indian Ocean, *J. Phys. Oceanogr.*, *35*, 708–728.

Han, W., D. M. Lawrence, and P. J. Webster (2001), Dynamical response of equatorial Indian Ocean to intraseasonal winds: Zonal flow, *Geophys. Res. Lett.*, *28*, 4215–4218.

Han, W., P. J. Webster, R. Lukas, P. Hacker, and A. Hu (2004), Impact of atmospheric intraseasonal variability in the Indian Ocean: Low-frequency rectification in equatorial surface current and transport, *J. Phys. Oceanogr.*, *34*, 1350–1372.

Han, W. Q., D. L. Yuan, W. T. Liu, and D. J. Halkides (2007), Intraseasonal variability of Indian Ocean sea surface temperature during boreal winter: Madden-Julian Oscillation versus submonthly forcing and processes, *J. Geophys. Res.*, *112*, C04001, doi:10.1029/2007JC004544.

Hendon, H. H., and J. Glick (1997), Intraseasonal air-sea interaction in the tropical Indian and Pacific Oceans, *J Clim.*, *10*(4), 647–661.

Izumo, T., et al. (2010), Influence of the state of the Indian Ocean dipole on the following year's El Niño, *Nat. Geosci.*, *3*, 168–172.

Iskandar, I., W. Mardiansyah, Y. Masumoto, and T. Yamagata (2005), Intraseasonal Kelvin waves along the southern coast of Sumatra and Java, *J. Geophys. Res.*, *110*, C04013, doi:10.1029/2004JC002508.

Iskandar, I., T. Tozuka, H. Sasaki, Y. Masumoto, and T. Yamagata (2006), Intraseasonal variations of surface and subsurface currents off Java as simulated in a high-resolution ocean general circulation model, *J. Geophys. Res.*, *111*, C12015, doi:10.1029/2006JC003486.

Iskandar, I., H. Sasaki, Y. Sasai, Y. Masumoto, and K. Mizuno (2010). A numerical investigation of eddy-induced chlorophyll bloom in the southeastern tropical Indian Ocean during Indian Ocean Dipole—2006. *Ocean Dyn.*, *60*(3), 731–742.

Jayakumar, A., J. Vialard, M. Lengaigne, C. Gnanaseelan, J. P. McCreary, and B. P. Kumar (2011), Processes controlling the surface temperature signature of the Madden-Julian Oscillation in the thermocline ridge of the Indian Ocean, *Clim. Dyn.*, *37*(11–12), 2217–2234.

Justice, C. O., E. Vermote, J. R. Townshend, R. Defries, D. P. Roy, D. K. Hall, V. V. Salomonson, J. L. Privette, G. Riggs, and A. Strahler (1998), The Moderate Resolution Imaging Spectroradiometer (MODIS): Land remote sensing for global change research, *IEEE Trans. Geosci. Remote Sens.*, *36*(4), 1228–1249.

Kawamiya, M., and A. Oschlies (2001), Formation of a basin-scale surface chlorophyll pattern by Rossby waves, *Geophys. Res. Lett.*, *28*(21), 4139–4142.

Kim, S. T., J. Y. Yu, and M. M. Lu (2012), The distinct behaviors of Pacific and Indian Ocean warm pool properties on seasonal and interannual time scales, *J. Geophys. Res.*, *117*, D05128, doi:10.1029/2011jd016557.

Kummerow, C., W. Barnes, T. Kozu, J. Shiue, and J. Simpson (1998), The Tropical Rainfall Measuring Mission (TRMM) sensor package, *J. Atmos. Oceanic Technol.*, *15*(3), 809–817.

Le Traon, P. Y., F. Nadal, and N. Ducet (1998), An improved mapping method of multisatellite altimeter data, *J. Atmos. Oceanic Technol*, *15*(2), 522–534.

Li, Y., W. Han, T. Shinoda, C. Wang, R. C. Lien, J. N. Moum, and J. W. Wang (2013), Effects of the diurnal cycle in solar radiation on the tropical Indian Ocean mixed layer variability during wintertime Madden-Julian Oscillations, *J. Geophys. Res. Oceans*, *118*, 4945–4964 doi:10.1002/jgrc.20395.

Li, Y., W. Han, T. Shinoda, C. Wang, M. Ravichandran, and J. Wang (2014), Revisiting the wintertime intraseasonal SST variability in the tropical South Indian Ocean: Impact of the ocean interannual variation, *J. Phys. Oceanogr.*, *44*(7), 1886–1907.

Li, Y., W. Han, and T. Lee (2015), Intraseasonal sea surface salinity variability in the equatorial Indo-Pacific Ocean induced by Madden-Julian oscillations, *J. Geophys. Res. Oceans*, *120*, 2233–2258, doi:10.1002/2014JC010647.

Liebmann, B., and C. A. Smith (1996), Description of a complete (interpolated) outgoing longwave radiation dataset, *Bull. Am. Meteorol. Soc.*, *77*(6), 1275–1277.

Madden, R. A., and P. R. Julian (1971), Detection of a 40-50 day oscillation in the zonal wind in the tropical Pacific, *J. Atmos. Sci.*, *28*(5), 702–708.

McCreary, J. P., Jr., P. K. Kundu, and R. L. Molinari (1993), A numerical investigation of dynamics, thermodynamics and mixed-layer processes in the Indian Ocean, *Prog. Oceanogr.*, *31*, 181–244.

McPhaden, M. J. (1982), Variability in the central equatorial Indian Ocean. Part 1: Ocean dynamics, *J. Mar. Res.*, *40*, 157–176.

McPhaden, M. J., and G. R. Foltz (2013), Intraseasonal variations in the surface layer heat balance of the central equatorial Indian Ocean: The importance of zonal advection and vertical mixing, *Geophys. Res. Lett.*, *40*, 2737–2741, doi:10.1002/grl.50536.

Murtugudde, R., and A. J. Busalacchi (1999), Interannual variability of the dynamics and thermodynamics, and mixed layer processes in the Indian Ocean, *J. Clim.*, *12*, 2300–2326.

Murtugudde, R., J. P. McCreary, and A. J. Busalacchi (2000), Oceanic processes associated with anomalous events in the Indian Ocean with relevance to 1997–1998, *J. Geophys. Res.*, *105*(C2), 3295–3306.
Pujiana, K., A. L. Gordon, and J. Sprintall (2013), Intraseasonal Kelvin wave in Makassar Strait, *J. Geophys. Res. Oceans*, *118*, 2023–2034, doi:10.1002/jgrc.20069.
Qiu, B., M. Mao, and Y. Kashino (1999), Intraseasonal variability in the Indo-Pacific throughflow and the regions surrounding the Indonesian seas, *J. Phys. Oceanogr.*, *29*, 1599–1618.
Reppin, J., F. A. Schott, J. Fischer, and D. Quadfasel (1999), Equatorial currents and transports in the upper central Indian Ocean: Annual cycle and interannual variability. *J. Geophys. Res.*, *104*(C7), 15,495–15,514.
Saji, N. H., B. N. Goswami, P. N. Vinayachandran, and T. Yamagata (1999), A dipole mode in the tropical Indian Ocean, *Nature*, *401*(6751), 360–363, doi:10.1038/43855.
Saji, N. H., S. P. Xie, and C. Y. Tam (2006), Satellite observations of intense intraseasonal cooling events in the tropical south Indian Ocean, *Geophys. Res. Lett.*, *33*, L14704, doi:10.1029/2006GL026525.
Sardeshmukh, P. D., and B. J. Hoskins (1988), The generation of global rotational flow by steady idealized tropical divergence, *J. Atmos. Sci.*, *45*(7), 1228–1251.
Schiller, A., and J. S. Godfrey (2003), Indian Ocean intraseasonal variability in an ocean general circulation model. *J. Clim.*, *16*, 21–39.
Schiller, A., S. E. Wijffels, J. Sprintall, R. Molcard, and P. R. Oke (2010), Pathways of intraseasonal variability in the Indonesian throughflow region, *Dyn. Atmos. Oceans*, *50*, 174–200.
Schott, F. A., S.-P. Xie, and J. P. McCreary Jr. (2009), Indian Ocean circulation and climate variability, *Rev. Geophys.*, *47*, RG1002, doi:10.1029/2007RG000245.
Schouten, M. W., W. P. M. de Ruijter, P. J. van Leeuwin, and H. A. Dijkstra (2002), An oceanic teleconnection between the equatorial and southern Indian Ocean, *Geophys. Res. Lett.*, *29*(16), 1812, doi:10.1029/2001GL014542.
Senan, R., D. Sengupta, and B. N. Goswami (2003), Intraseasonal monsoon jets in the equatorial Indian Ocean, *Geophys. Res. Lett.*, *30*(14), 1750, doi:10.1029/2003GL017583.
Sengupta, D., R. Senan, and B. N. Goswami (2001), Origin of intraseasonal variability of circulation in the tropical central Indian Ocean, *Geophys. Res. Lett.*, *28*, 1267–1270.
Shinoda, T., and H. H. Hendon (1998), Mixed layer modeling of intraseasonal variability in the tropical western Pacific and Indian Oceans, *J. Clim.*, *11*, 2668–2685.
Shinoda, T., H. H. Hendon, and J. Glick (1998), Intraseasonal variability of surface fluxes and sea surface temperature in the tropical western Pacific and Indian Oceans, *J. Clim.*, *11*, 1685–1702.
Susanto, R. D., A. L. Gordon, and Q. N. Zheng (2001), Upwelling along the coasts of Java and Sumatra sand its relation to ENSO, *Geophys. Res. Lett.*, *28*(8), 1599–1602.
Vinayachandran, P. N., and N. H. Saji (2008), Mechanisms of South Indian Ocean intraseasonal cooling, *Geophys. Res. Lett.*, *35*, L23607, doi:10.1029/2008GL035733.
Vinayachandran, P. N., C. P. Neema, S. Mathew, and R. Remya (2012), Mechanisms of summer intraseasonal sea surface temperature oscillations in the Bay of Bengal, *J. Geophys. Res.*, *117*, C01005, doi:10.1029/2011JC007433.
Waliser, D. E., R. Murtugudde, and L. E. Lucas (2003), Indo-Pacific Ocean response to atmospheric intraseasonal variability. Part I: Austral summer and the Madden–Julian oscillation, *J. Geophys. Res.*, *108*(C5), 3160, doi:10.1029/2002JC001620.
Waliser, D. E., R. Murtugudde, and L. E. Lucas (2004), Indo-Pacific ocean response to atmospheric intraseasonal variability. Part II: Boreal summer and the intraseasonal oscillation. *J. Geophys. Res.*, *109*, C03030, doi:10.1029/2003JC002002.
Wang, H., and V. Mehta (2008), Decadal variability of the Indo-Pacific Warm pool and its association with atmospheric and oceanic variability in the NCEP–NCAR and SODA reanalyses, *J. Clim.*, *21*, 5545–5565.
Webber, B. G. M., D. P. Stevens, A. J. Matthews, and K. J. Heywood (2012), Dynamical ocean forcing of the Madden-Julian oscillation at lead times of up to five months, *J Clim.*, *25*(8), 2824–2842, doi:10.1175/Jcli-D-11-00268.1.
Webster, P. J., and R. Lukas (1992), TOGA COARE: The coupled ocean atmosphere response experiment, *Bull. Am. Meteorol. Soc.*, *73*(9), 1377–1416.
Webster, P. J., A. M. Moore, J. P. Loschnigg, and R. R. Leben (1999), Coupled ocean-atmosphere dynamics in the Indian Ocean during 1997-98, *Nature*, *401*(6751), 356–360.
Webster, P. J., et al. (2002), The jasmine pilot study, *Bull. Am. Meteorol. Soc.*, *83*(11), 1603–1630, doi:10.1175/BAMS-83-11-1603.
Wentz, F. J., C. Gentemann, D. Smith, and D. Chelton (2000), Satellite measurements of sea surface temperature through clouds, *Science*, *288*(5467), 847–850.
Wielicki, B. A., B. R. Barkstrom, E. F. Harrison, R. B. Lee, G. L. Smith, and J. E. Cooper (1996), Clouds and the earth's radiant energy system (CERES): An earth observing system experiment, *Bull. Am. Meteorol. Soc.*, *77*(5), 853–868.
Wyrtki, K. (1973), An equatorial jet in the Indian Ocean, *Science*, *181*, 262–264.
Yu, J.-Y., C. R. Mechoso, J. C. McWilliams, and A. Arakawa (2002), Impacts of the Indian Ocean on the ENSO cycle, *Geophys. Res. Lett.*, *29*(8), 1204, doi:10.1029/2001GL014098.
Zelle, H., G. Appeldoorn, G. Burgers, and G. J. van Oldenborgh (2004), The relationship between sea surface temperature and thermocline depth in the eastern equatorial Pacific, *J. Phys. Oceanogr.*, *34*(3), 643–655.
Zhang, C. (2005), Madden-Julian oscillation, *Rev. Geophys.*, *43*, RG2003, doi:10.1029/2004RG000158.